Available online at www.sciencedirect.com
SCIENCE DIRECT®
Optics Communications 231 (2004) 137–147
OPTICS COMMUNICATIONS
www.elsevier.com/locate/optcom

Jones vector imaging by use of digital holography: simulation and experimentation

T. Colomb [a,*], E. Cuche [a,b], F. Montfort [a], P. Marquet [c], Ch. Depeursinge [a]

[a] *STI/BIO-E/LOA, Swiss Federal Institute of Technology, CH-1015 Lausanne, Switzerland*
[b] *Lyncée Tec SA, Rue du Bugnon 7, CH-1005 Lausanne, Switzerland*
[c] *Department of Neurology, Laboratory of Neurological Research, Institute of Physiology, University of Lausanne, CH-1015 Lausanne, Switzerland*

Received 17 September 2003; received in revised form 28 November 2003; accepted 1 December 2003

Abstract

We present a method to image Jones vector by use of digital holography. We demonstrate that with a single hologram acquisition, the method allows to image and to calculate Jones vector and derive the polarization parameters. The principle consists in using two reference waves polarized orthogonally that interfere with an object wave and to reconstruct separately the two wave fronts. Simulated and experimental data are compared to a theoretical model in order to evaluate the precision limit of the method for different polarization states of the object wave.

PACS: 42.25.Ja; 42.40.-I; 42.30.−d

Keywords: Digital holography; Polarization; Birefringence imaging; Jones vector

1. Introduction

Polarization studies can be divided into two categories: those for measuring the time dependence of the state of polarization (SOP) [1] and those for measuring the space dependence [2,3]. The main difficulty rises from the fact that very few techniques allow for simultaneous record of SOP parameters. Indeed, most polarimetric techniques need polarization-analyzing optics (polarizers, rotators and retarders) that must be used at various settings to record several images, from which SOP parameters can be determined using more or less complicated algorithms. Such procedures require generally several rotations of the analyzing optics that takes a long time compared to the acquisition performances of a charge coupled device (CCD) camera. A solution was given by Oldenbourg and Mei [4], who used a liquid-crystal universal compensator to improve the temporal resolution. Another idea is to record all SOP parameters with only one image acquisition. Therefore the time-resolution depends only on the camera characteristics. Oka et al. adopted birefringent wedge prisms to record the SOP Stokes

* Corresponding author. Tel.: +41216933742; fax: +41216933701.
E-mail address: tristan.colomb@epfl.ch (T. Colomb).

0030-4018/$ - see front matter © 2003 Elsevier B.V. All rights reserved.
doi:10.1016/j.optcom.2003.12.004

parameters carried on fringes patterns having different spatial frequencies. A demodulation of the obtained image using Fourier transform allows to compute the Stokes parameters [5]. An older idea presented by Ohtsuka and Oka [6] used a Mach–Zender type interferometer to record an interferogram resulting from the interference between an object wave, and two orthogonal linearly polarized reference waves. The resulting interference pattern is then collected by a lens in order to focus an image of the specimen on the CCD. Here also, a Fourier based analysis provides the SOP parameters.

The method proposed here is very similar to the last one, since we also use two orthogonal linearly polarized reference waves. But according to the principle of digital holographic imaging presented in [7] the main difference comes from the fact that the imaging lens can be suppressed. The interference between the two reference waves and the object wave provides a hologram recorded in an off-axis geometry. Instead of using a Fourier transform to calculate the SOP parameters, the hologram is reconstructed in amplitude and phase for each polarization components by computing the illumination of the hologram by digital reference waves as explained in [7]. From one hologram, the numerical reconstruction process gives four images, two (amplitude and phase) for each orthogonally polarized reference wave. From this set of images, a quantitative evaluation of the 2D distribution of the Jones vector parameters can be performed [8]. In this paper numerical simulations and experimental data are compared to a theoretical model in order to evaluate the precision and the limitations of the method.

2. Theory

The wave polarization properties can be expressed by use of the Jones formalism [9]. The SOP is expressed by the Jones vector associated to a base xyz where z is along the wave propagation direction and x and y are fixed by the operator. The Jones vector of a wave $\boldsymbol{E}$ can be written as

$$\boldsymbol{J_E} = \begin{pmatrix} e_1 \\ e_2 \end{pmatrix} = \begin{pmatrix} e'_1 \\ e'_2\, \mathrm{e}^{\mathrm{i}\Delta\varphi_E} \end{pmatrix}, \tag{1}$$

where e_1 and e_2 are complex. Instead of four parameters as in Eq. (1) (two amplitude and two phase parameters), the SOP can be expressed with only two parameters $\varepsilon = \arctan(e'_2/e'_1)$, where $e'_1 = |e_1|$ and $e'_2 = |e_2|$ are, respectively, the amplitude of e_1 and e_2, ε is the azimuth of the polarization ellipse and $\Delta\varphi_E = \mathrm{phase}(e_2) - \mathrm{phase}(e_1)$ is the phase difference. To simplify the notation we use the complex values e_1 and e_2.

A modified Mach–Zender set-up (Fig. 1(a)) allows creating holograms in off-axes geometry, by producing the interference between an object wave $\boldsymbol{O}$ and two orthogonal linear polarized waves $\boldsymbol{R}_1$ and $\boldsymbol{R}_2$ coming from two different spatial directions (Fig. 1(b)). The respective Jones vectors of $\boldsymbol{O}$, $\boldsymbol{R}_1$ and $\boldsymbol{R}_2$ associated to their respective basis are:

$$\begin{aligned}
\boldsymbol{J_O} &= \begin{pmatrix} o_1 \\ o_2 \end{pmatrix}_{(xy)\boldsymbol{O}} = \begin{pmatrix} o_1 \\ o_2 \\ 0 \end{pmatrix}_{(xyz)\boldsymbol{O}}, \\
\boldsymbol{J_{R_1}} &= \begin{pmatrix} r_1 \\ 0 \end{pmatrix}_{(xy)\boldsymbol{R}_1} = \begin{pmatrix} r_1 \\ 0 \\ 0 \end{pmatrix}_{(xyz)_{\boldsymbol{R}_1}}, \\
\boldsymbol{J_{R_2}} &= \begin{pmatrix} 0 \\ r_2 \end{pmatrix}_{(xy)\boldsymbol{R}_2} = \begin{pmatrix} 0 \\ r_2 \\ 0 \end{pmatrix}_{(xyz)\boldsymbol{R}_2}.
\end{aligned} \tag{2}$$

For each base, the off-axis geometry defines the z direction and the operator defines the x and y directions by adjusting polarizers. To avoid any interference between reference waves, $x_{\boldsymbol{R}_1}$ and $y_{\boldsymbol{R}_2}$ should be orthogonal. Moreover, $x_{\boldsymbol{O}}$ and $y_{\boldsymbol{O}}$ should be orthogonal to, respectively, $x_{\boldsymbol{R}_1}$ and $y_{\boldsymbol{R}_2}$ to avoid any interference between o_1 and r_2, and o_2 and r_1. Therefore, the planes (dashed rectangles in Fig. 1(b)) $x_{\boldsymbol{O}}z_{\boldsymbol{O}}$ (containing $\boldsymbol{O}$ and $\boldsymbol{R}_2$) $y_{\boldsymbol{O}}z_{\boldsymbol{O}}$ (containing $\boldsymbol{O}$ and $\boldsymbol{R}_1$) are orthogonal. The angles θ_1 and θ_2, as defined in Fig. 1(b), are the experimental parameters that define the two different propagation directions of the reference waves. Satisfying all these conditions and assuming plane waves, the different waves are written in $(xyz)_O$ base as

$$\boldsymbol{O} = \boldsymbol{J_O}\,\mathrm{e}^{\mathrm{i}(\boldsymbol{k_O r} + \phi_{\mathrm{O}}(x,y))}, \quad \boldsymbol{R}_1 = \boldsymbol{J_{R_1}}\,\mathrm{e}^{\mathrm{i}\boldsymbol{k}_1\boldsymbol{r}}, \quad \boldsymbol{R}_2 = \boldsymbol{J_{R_2}}\mathrm{e}^{\mathrm{i}\boldsymbol{k}_2\boldsymbol{r}}, \tag{3}$$

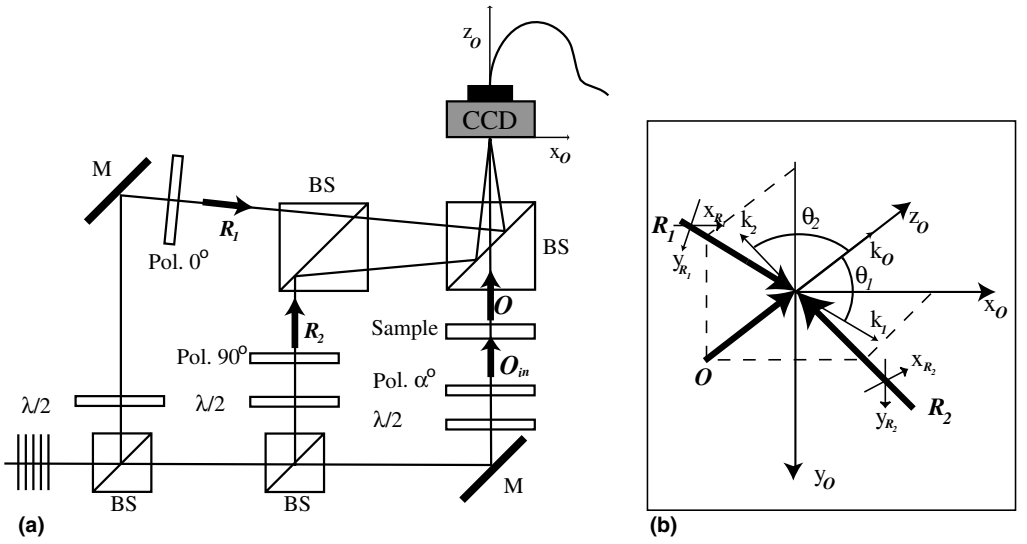

Fig. 1. (a) Experimental set-up: $\boldsymbol{O}_{\text{in}}$ – illuminating wave; $\boldsymbol{O}$ – object wave; $\boldsymbol{R}_1$ and $\boldsymbol{R}_2$ – polarized reference waves; Pol. α° – polarizer oriented at α°; $\lambda/2$ – half wave plate; M – mirror; BS – beam splitter. (b) Detail showing the off-axis geometry at the incidence on the CCD. The $x_O y_O$ plane is parallel to the CCD camera. $\boldsymbol{R}_1$ in the $y_O z_O$ plane and $\boldsymbol{R}_2$ in the $x_O z_O$ plane are coming from different spatial directions.

where $\boldsymbol{r} = (x, y, z)$ is the position vector, $\phi_{\text{O}}(x, y)$ is the phase delay induced by the sample topography. The wave vectors are written

$$\boldsymbol{k_O} = \frac{2\pi}{\lambda}\begin{bmatrix}0\\0\\1\end{bmatrix}, \quad \boldsymbol{k}_1 = \frac{2\pi}{\lambda}\begin{bmatrix}0\\\sin(\theta_1)\\\cos(\theta_1)\end{bmatrix},$$
$$\boldsymbol{k}_2 = \frac{2\pi}{\lambda}\begin{bmatrix}-\sin(\theta_2)\\0\\\cos(\theta_2)\end{bmatrix}. \tag{4}$$

where λ is the wavelength of the laser used.

Now, a hologram of $N \times N$ points can be performed by simulating the interference between these three waves in the plane $z = 0$ and by integrating on one pixel size

$$I_{\text{H}}(i,j) = \int_{i\overline{x}-(\overline{x}/2)}^{i\overline{x}+(\overline{x}/2)} \int_{j\overline{y}-(\overline{y}/2)}^{j\overline{y}+(\overline{y}/2)} (\boldsymbol{R}_1 + \boldsymbol{R}_2 + \boldsymbol{O}) \times (\boldsymbol{R}_1 + \boldsymbol{R}_2 + \boldsymbol{O})^* \,\mathrm{d}x\,\mathrm{d}y, \tag{5}$$

where i, j are integers ($-N/2 \leqslant i,\ j < N/2$) and $\overline{x} = \overline{y}$ is the pixel size of CCD camera. Assuming that the waves are plane, it is possible to find an analytic solution to this integral. Hence, "perfect" holograms can be achieved (perfect in sense that we take into account the pixel size when integrating and we assume that holograms have no noise).

Without a priori knowledge, the hologram intensity defined in Eq. (5) can be written as

$$\begin{aligned} I_{\text{H}}(x,y) &= (\boldsymbol{R}_1 + \boldsymbol{R}_2 + \boldsymbol{O})(\boldsymbol{R}_1 + \boldsymbol{R}_2 + \boldsymbol{O})^* \\ &= |\boldsymbol{R}_1|^2 + |\boldsymbol{R}_2|^2 + |\boldsymbol{O}|^2 + \boldsymbol{R}_1\boldsymbol{O}^* \\ &\quad + \boldsymbol{R}_2\boldsymbol{O}^* + \boldsymbol{R}_1^*\boldsymbol{O} + \boldsymbol{R}_2^*\boldsymbol{O}. \end{aligned} \tag{6}$$

The three first terms of Eq. (6) form the zero order of diffraction; the fourth and fifth terms produce two real images corresponding, respectively, to linear horizontal and vertical SOP. The last two terms produce the virtual images.

To reconstruct the SOP images of the object wave, the algorithm presented in [7] and adapted in [8] is used. It consists in simulating the standard optical reconstruction of hologram. In classical holography, reconstruction is achieved by illumination of the hologram with a replica of the reference wave. A wave front $\Psi(x,y) = \boldsymbol{R}(x,y) I_{\text{H}}(x,y)$ is transmitted by the hologram and propagates toward an observation plane, where a three-dimensional image of the object can be observed. Here as

we reconstruct a digital hologram, a digital transmitted wave front $\Psi(i\bar{x}, j\bar{y})$ is computed by multiplication of digital hologram $I_H(i,j)$ by a digitally computed reference wave $\boldsymbol{R}_D(i,j)$, called the digital reference wave. Assuming we are dealing with plane waves, $\boldsymbol{R}_D$ can be calculated as follows:

$$\boldsymbol{R}_D = \exp\left[\left(k_{Dx} i\bar{x} + k_{Dy} j\bar{y}\right)\right], \tag{7}$$

where k_{Dx}, and k_{Dy} are the two components of the wave vector. The digital transmitted wave front $\Psi(i\bar{x}, j\bar{y})$ is defined in the hologram plane $x_O y_O$. The propagation of the wave front Ψ is simulated by a numerical calculation of scalar diffraction in the Fresnel approximation. The reconstructed wave front $\Psi(m\Delta\xi, n\Delta\eta)$, at a distance d from the hologram plane, in an observation plane $O\xi\eta$, is computed by use of a discrete expression of the Fresnel integral

$$\begin{aligned}&\Psi(m\Delta\xi, n\Delta\eta)\\ &= A\exp\left[\frac{\mathrm{i}\pi}{\lambda d}\left(m^2\Delta\xi^2 + n^2\Delta\eta^2\right)\right]\\ &\quad\times \mathrm{FFT}\left\{\boldsymbol{R}_D(i,j) I_H(i,j)\exp\left[\frac{\mathrm{i}\pi}{\lambda d}\left(i^2\bar{x}^2 + j^2\bar{y}^2\right)\right]\right\}_{m,n},\end{aligned} \tag{8}$$

where m and n are integers ($-N/2 \leqslant m,\ n < N/2$), FFT is the Fast Fourier Transform operator, and $A = \exp(\mathrm{i}2\pi d/\lambda)/(i\lambda d)$. $\Delta\xi$ and $\Delta\eta$ are the sampling intervals in the observation plane.

Considering only the virtual images of Eq. (6), the wave fronts corresponding to the two respective digital reference waves are:

$$\begin{aligned}&\Psi_1 = \boldsymbol{R}_{D1}\boldsymbol{R}_1^* O, \quad \boldsymbol{R}_{D1} = \exp(k_{D1x}\cdot i\bar{x} + k_{D1y}\cdot j\bar{y}),\\ &\Psi_2 = \boldsymbol{R}_{D2}\boldsymbol{R}_2^* \boldsymbol{O}, \quad \boldsymbol{R}_{D2} = \exp(k_{D2x}\cdot i\bar{x} + k_{D2y}\cdot j\bar{y}),\end{aligned} \tag{9}$$

where k_{D1x}, k_{D1y}, k_{D2x}, k_{D2y} are four parameters adjusted to achieve identical propagation directions for $\boldsymbol{R}_i$ and $\boldsymbol{R}_{Di}$ ($i = 1, 2$). The off-axis geometry allows separating the different orders, therefore the different areas corresponding to Ψ_1 and Ψ_2 can be selected on the reconstruction plane. Using Eqs. (2) and (3) in Eq. (9) and taking the amplitude and the phase of Ψ_1 and Ψ_2 gives:

$$\begin{aligned}&|\Psi_1| = |r_1 o_1| = |r_1||o_1|,\\ &\quad \mathrm{phase}(\Psi_1) = \mathrm{phase}(o_1) - \mathrm{phase}(r_1) + \phi_O,\\ &|\Psi_2| = |r_2 o_2| = |r_2||o_2|,\\ &\quad \mathrm{phase}(\Psi_2) = \mathrm{phase}(o_2) - \mathrm{phase}(r_2) + \phi_O.\end{aligned} \tag{10}$$

Assuming $|r_1| = |r_2|$, the phase difference $\Delta\varphi_{\boldsymbol{O}}$ and the azimuth ε parameters can be expressed from Eq. (10):

$$\begin{aligned}&\tan(\varepsilon) = \frac{|\Psi_2|}{|\Psi_1|} = \frac{|o_2|}{|o_1|},\\ &\Delta\varphi_{\boldsymbol{O}} = \mathrm{phase}(\Psi_2) - \mathrm{phase}(\Psi_1) + \Delta\varphi_{\boldsymbol{R}},\end{aligned} \tag{11}$$

where $\Delta\varphi_{\boldsymbol{R}} = \mathrm{phase}(r_2) - \mathrm{phase}(r_1)$ can be cancelled by a calibrated phase difference offset applied to the phase difference image. Experimentally, this term is time-dependent because of vibrations, air flux, but it can be suppressed on the image by a phase difference offset equal to $-\Delta\varphi_{\boldsymbol{R}}$. To adjust this offset, a known polarization state area is used in the image. For example a polarizer, that produces a phase difference of 0°, is placed in the object wave as shown in Fig. 2. Therefore a measurement of the mean phase difference in this area directly gives $\Delta\varphi_{\boldsymbol{R}}$.

To evaluate the reconstruction algorithm, we simulate some series of holograms resulting from the interference between the reference waves and the object wave of a known SOP. Then, we compare the theoretical values with those calculated by the hologram reconstruction. The input object wave $\boldsymbol{O}_{in}$ is chosen (wave in the object arm before transmission through the sample) as a linear

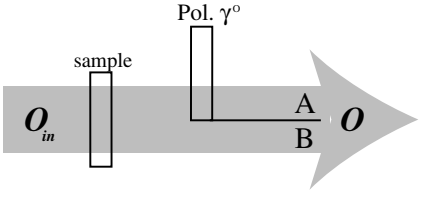

Fig. 2. Use of reference area in the object arm. $\boldsymbol{O}_{in}$ – illuminating wave, Pol. γ – polarizer oriented at angle γ, used as reference area for the phase difference offset determination. A is the reference area where phase difference is 0 and B the area where the measurement of $\boldsymbol{O}$ is done.

polarization oriented at 45° (in Fig. 1 polarizer angle $\alpha = 45°$), the Jones vector of this wave is

$$\boldsymbol{J}_{\boldsymbol{O}_{\text{in}}} = \begin{pmatrix} 1 \\ 1 \end{pmatrix}. \tag{12}$$

Then, a half wave plate is used as sample and different holograms are simulated (or recorded) for different orientations of it. A wave retarder with an orientation δ is represented by the Jones matrix

$$T(\delta) = R(-\delta)\begin{bmatrix} 1 & 0 \\ 0 & \exp(-\mathrm{i}\Gamma) \end{bmatrix} R(\delta), \tag{13}$$

where $\Gamma = \pi$ for half wave retarder. R is the matrix of the coordinates transformation

$$R(\delta) = \begin{bmatrix} \cos(\delta) & \sin(\delta) \\ -\sin(\delta) & \cos(\delta) \end{bmatrix}. \tag{14}$$

Therefore, the Jones vector of $\boldsymbol{O}$ becomes

$$\boldsymbol{J}_{\boldsymbol{O}} = T(\delta)\boldsymbol{J}_{\boldsymbol{O}_{\text{in}}}. \tag{15}$$

The results compare the theoretical SOP of $\boldsymbol{J}_{\boldsymbol{O}}$, with the parameters obtained by the reconstruction of the simulated holograms and finally with the parameters obtained by the reconstruction of the experimental holograms.

3. Results and discussion

For the simulation, the actual parameters measured on the set-up are used. The laser is a He–Ne with a wavelength of 632.8 nm. The angles between each reference wave and the object wave are $\theta_1 = \theta_2 = 0.72°$ and the pixel size of the CCD camera used (Hitashi KP-M2 CCIR) is 8.6 μm. These parameters allow simulating $N \times N$ holograms with Eq. (5). The reconstruction algorithm uses usually 512×512 pixels holograms, but for comparison 256×256 pixels holograms are presented in Fig. 3.

In Fig. 4 the amplitude and the phase contrasts of the reconstructed wave fronts are presented. For the experimental reconstruction, a polarizer is introduced as a reference area (A in Fig. 4) as explained in the last chapter (Fig. 2). Computing pixel per pixel the inverse tangent of the quotient of the second image by the first one yields the azimuth ε image and computing the difference between the fourth and the third gives the phase difference image $\Delta\varphi_{\boldsymbol{O}}$. The results are presented in Fig. 5.

Simulating or recording holograms for different orientations of a half wave plate used as sample (0° to 180° by 1° step) permits to compare theoretical SOP and reconstructed SOP mean value calculated in regions of interest (ROI defined by solid rectangles in Fig. 5) of reconstructed images. To determine the phase difference with the experimental holograms, the phase difference offset is calculated as explained before by using the mean value in the ROI of the reference area (dashed rectangle in

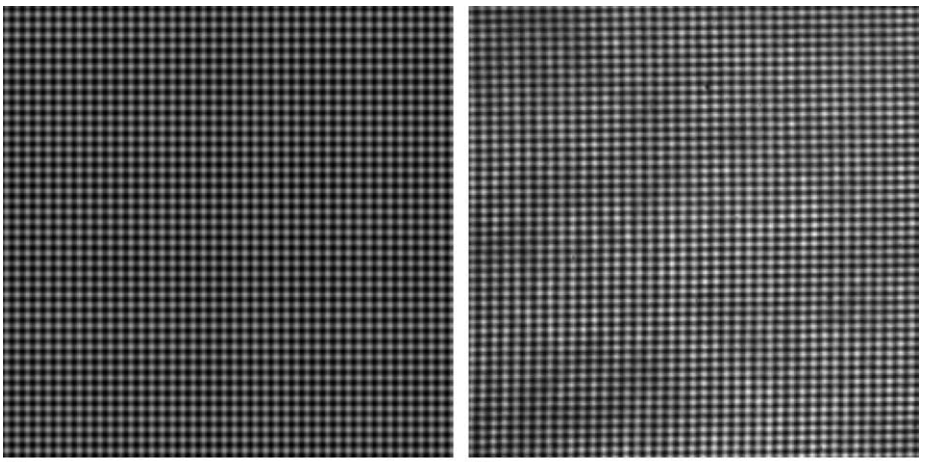

Fig. 3. Comparison between (a) simulated hologram and (b) experimental hologram.

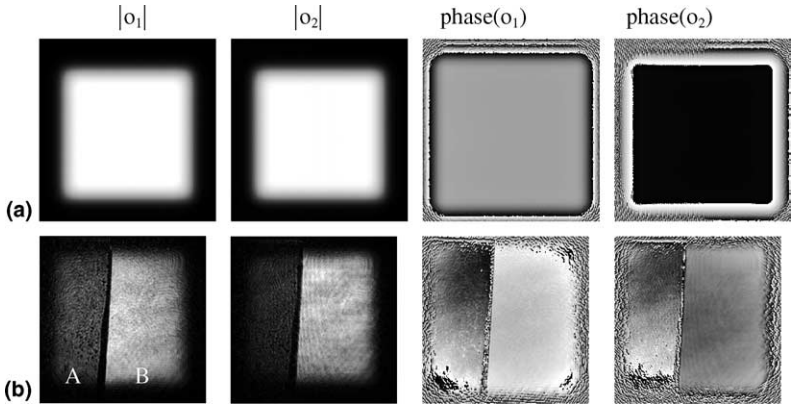

Fig. 4. Amplitude and phase contrasts reconstructed for (a) simulated hologram and (b) experimental hologram. In experimental images, the area A on the left is the polarizer and B the half wave plate.

Fig. 5). The result is presented in Fig. 6. An almost perfect superposition of the theoretical and simulated curves is achieved, while the experimental curves are in good agreement. To permit a better comparison, Fig. 7 presents the difference between theoretical and reconstructed SOP values. The precision of SOP parameters for a single pixel is evaluated by computing the standard deviation of SOP parameters in the same ROI (Fig. 8).

The graphs about mean values (Fig. 7) show that there is an important difference between errors for the simulated and errors for the experimental set-up (0.01° and 1° for the azimuth for, respectively, simulated and experimental set-up, and 0.03° and 5° for phase difference). However a similar behavior can be observed. The experimental results on the azimuth errors show four peaks (arrows in Fig. 7(a)), also observable on simulation results (fit in Fig. 7(a)). These four critical orientations of the half-wave plate correspond to a linear horizontal ($\delta = 22.5°$, $112.5°$) and vertical ($\delta = 67.5°$, $157.5°$) polarized object wave. For these orientations, the amplitude corresponding to an orthogonal polarization should be zero. Different contributions appearing in the image account for the observed amplitude offset. The first very low contribution comes from algorithm and will be called ''numerical noise''. It provides the explanation of the observed offset on simulations. The experimental set-up gives a higher offset amplitude component. Indeed the experimental holograms are disturbed by different noise sources. The first source is the ''structural noise'' coming from a coherent interference between parasitic waves (reflection on optics, diffraction on dust, etc.). The second one comes from the CCD camera which is affected by such as electronic noise, shot noise, dark noise and so on.

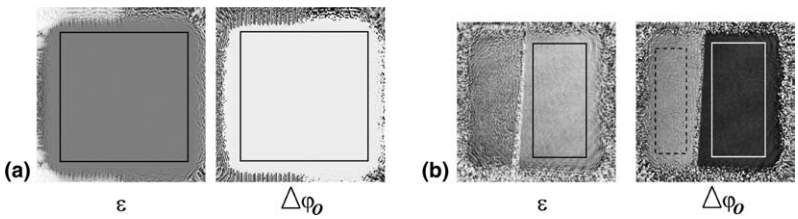

Fig. 5. Polarization parameters images for simulated hologram (a) and experimental hologram (b). The calculus of SOP mean values and standard deviations are calculated with pixel values inside the ROI defined by the solid rectangles. In case of experimental phase difference image, the mean value calculated in the dashed ROI permits to adjust the phase difference offset.

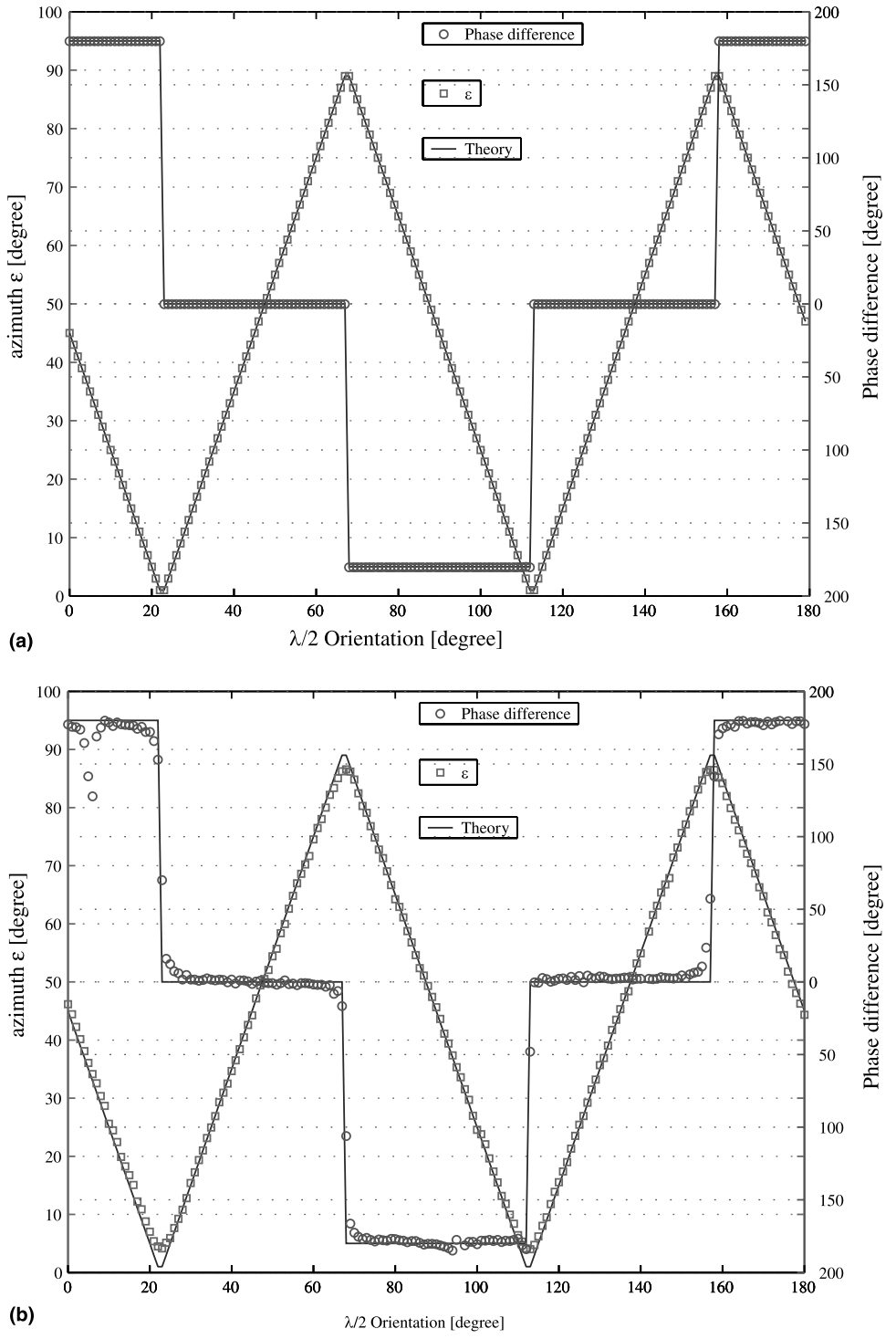

Fig. 6. Comparison between theory and (a) simulated reconstructed holograms and (b) experimental reconstructed holograms.

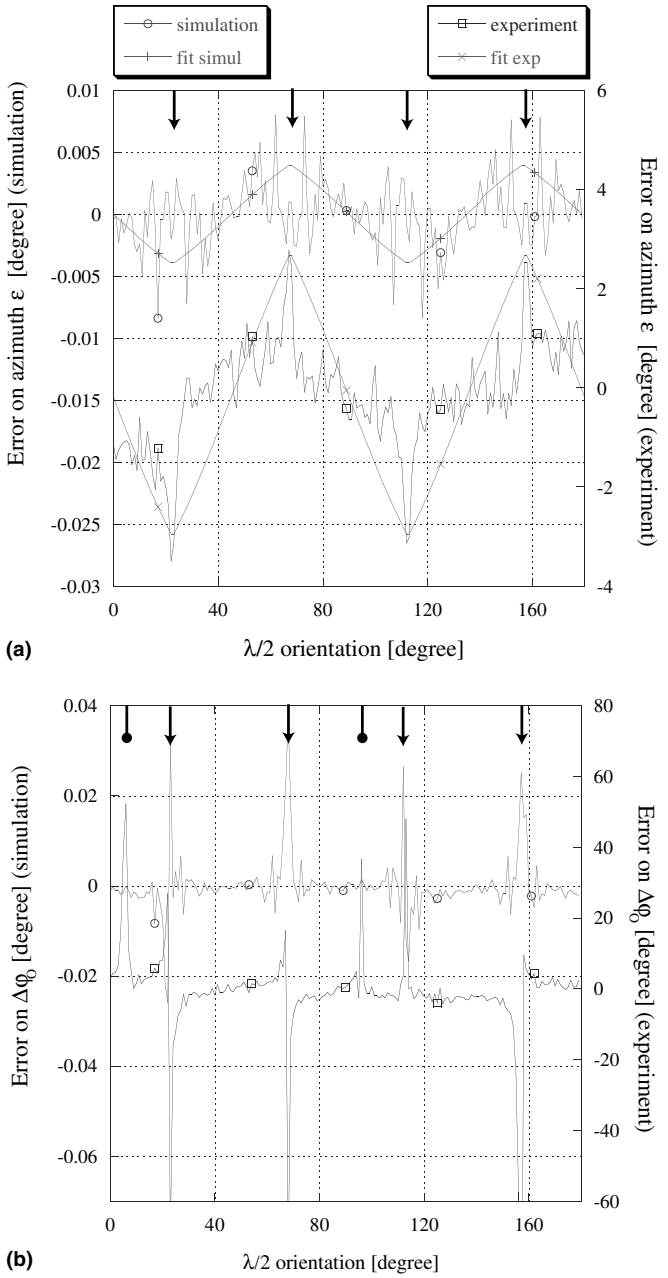

Fig. 7. Difference between theoretical values and SOP reconstructed values: (a) azimuth and (b) phase difference. The arrows indicate the critical angles for which the object wave is polarized vertically or horizontally. The arrows with the point indicate the critical angles for which no light is passing through the reference polarizer. The lines on part (a) of the figure fits errors on the azimuth after adjustment of the background amplitude for $|o_1|$ and $|o_2|$ for the experimental and simulated holograms cases.

Finally misalignments and small errors on the optics orientations are error sources. A simple model allows fitting the simulated and experimental values. Assuming an amplitude offset equal to a percentage α and β of respectively, maximum $|o_1|$ and $|o_2|$ amplitude, the azimuth error is written

$$\varepsilon_t - \varepsilon_c = \varepsilon_t - \arctan\left(\frac{|o_2| + \alpha \max(|o_2|)}{|o_1| + \beta \max(|o_1|)}\right), \quad (16)$$

where ε_t and ε_c are, respectively, the theoretical and calculated azimuth, and $\max(|o_i|)$, the maximum of amplitude for the object wave polarized horizontally ($i = 1$) or vertically ($i = 2$). Fits in Fig. 7(a) are plotted with $\alpha = \beta = 0.007\%$ for the simulation and $\alpha = 5\%$, $\beta = 5.5\%$ for the experimentation.

Rapid variations in experimental values can be explained by time instabilities mostly due to vibrations, air turbulence, that produces intensity variations for all interferences (interference between the object and reference waves and "structural noise"). For the simulation, truncated values in the algorithm can explain the rapid variation phenomena. A solution to avoid error due to the background is to calibrate the method by suppressing the background numerically before calculating azimuth. On the contrary it is difficult to suppress the errors due to the time instability.

The graph of the phase difference errors in Fig. 7(b) shows as expected a huge errors for the critical orientations (arrows in Fig. 7(b)). Indeed, for these orientations, the fringe pattern corresponding to the orthogonally polarized reference wave disappears. Therefore the algorithm can not reconstruct the phase image and a random phase image is obtained. The subtraction between the two phase contrasts contains also a random phase and an undefined phase difference is reconstructed. Moreover, a similar phenomenon (arrow with point in Fig. 7(b)) appears when the polarizer used as a reference area stops the input object wave. In this case, the reference area is undefined and therefore the phase difference offset cannot be calibrated.

The standard deviation on the images provides a mean of evaluating the quality of the imaging method. Fig. 8 shows that the limit of the algorithm is a standard deviation of about 0.12° for the azimuth and 0.3° for the phase difference (for an orientation different that the critical angles defined in the last paragraph). Experimentally, the limits are higher because of the same reasons explained before. For the azimuth measurement, Fig. 8(a) shows that experimentally the standard deviation is minimal for the critical angles. It can be understood with a simple error calculation

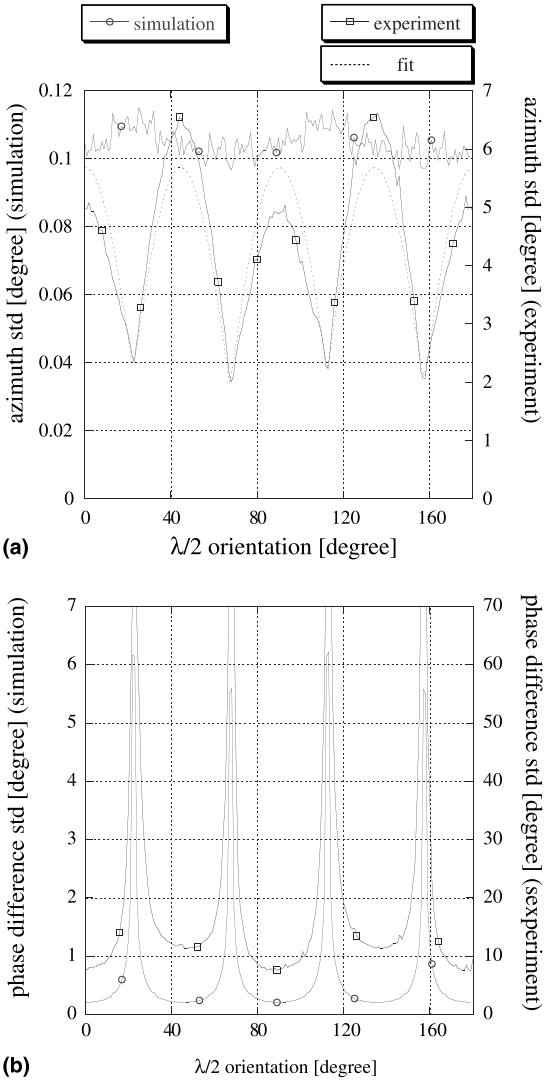

Fig. 8. Standard deviation of the polarization parameters for the measurement in object area: (a) azimuth and (b) phase difference.

$$\Delta\varepsilon = \frac{\Delta\varepsilon}{\partial|o_1|}\Delta|o_1| + \frac{\partial\varepsilon}{\partial|o_2|}\Delta|o_2| = \frac{|o_2|\Delta|o_1|}{|o_1|^2 + |o_2|^2} + \frac{|o_1|\Delta|o_2|}{|o_1|^2 + |o_2|^2}. \quad (17)$$

Fig. 9 shows a linear relation

$$\Delta|o_i| = \alpha_{i1} + \alpha_{i2}|o_i|. \quad (18)$$

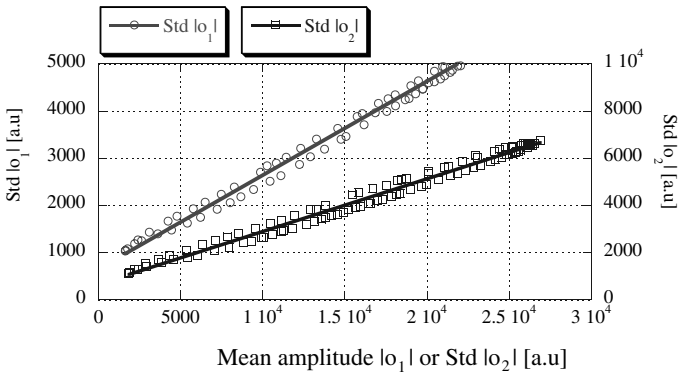

Fig. 9. Standard deviation for the amplitude contrasts versus mean amplitudes.

Using Eqs. (12)–(14) with $\Gamma = \pi$, a simple calculus gives

$$|o_1| = |\sin(2\delta) + \cos(2\delta)| \text{ and}$$
$$|o_2| = |\sin(2\delta) - \cos(2\delta)|. \quad (19)$$

Assuming $|o_1|^2 + |o_2|^2 = 1$ and introducing Eqs. (18) and (19) in Eq. (17) gives

$$\Delta\varepsilon = (\alpha_{12} + \alpha_{22})|\cos(4\delta)| + \alpha_{21}|\sin(2\delta) + \cos(2\delta)| + \alpha_{11}|\sin(2\delta) - \cos(2\delta)|. \quad (20)$$

The azimuth standard deviation is therefore minimal when $\cos(4\delta) = 0$ and therefore when $4\delta = 90 + n \times 180$ (n an integer). These orientations correspond to an object wave polarization orthogonal to one of the reference waves. The maximum standard deviation occurs when $4\delta = n \times 180$. An experimental data fit, plotted in dashed line in Fig. 8(a) with $\alpha_{12} + \alpha_{22} = 2.79$, $\alpha_{21} = 1.53$ and $\alpha_{11} = 1.35$, is well adapted for the critical angles. But the model does not explain the difference between the maximums that can be understood by a different quality of the reconstructed amplitude contrasts.

The phase difference standard deviation presents peaks for the critical angles for which random phase contrast is reconstructed for the orthogonal polarized component. Therefore, the phase difference has a high standard deviation. Between the critical angles, imperfect optics, dust and all noises expressed before give contributions to the phase difference standard deviation seen on the experimental reconstruction in Fig. 4. A quality difference between the two reconstructed phase images explains, as for the azimuth standard deviation, the different minimal values between the different critical orientations.

4. Conclusion

The estimation of errors made on calculated holograms demonstrates that the method is able to image and determine the SOP of an unknown object wave with about 0.01° for the azimuth and 0.03° for the phase difference out of the critical angles (when the object wave is polarized linearly horizontally or vertically). Moreover, it allows measuring the standard deviation limit introduced by the algorithm on the SOP images: 0.12° for the azimuth and 0.3° for the phase difference. Then the experimental holograms show that the method works well even if the errors are larger. We have demonstrated that with an only one image acquisition the method calculates the SOP parameters with an error smaller than 1° for the azimuth and smaller than 5° for the phase difference out of the critical angles. Set-up optimization, better optics and suppression of parasitic interferences by use of a low coherence source for example, would increase the precision. In conclusion, the method permits to record the spatiotemporal Jones vector of a specimen with a resolution time depending only on the CCD camera acquisition time. Moreover, even the spatial resolution in not yet very high, the introduction of a microscope objective should allow a spatial resolution smaller than 1 μm [10].

Acknowledgements

This work was funded through the research Grant No. 2153-067068.01 from the Swiss National Science Foundation and through the research Grant No. 6101-3, 6829.12 and 6606.2 of CTI program TOPNANO 21.

References

[1] G.E. Jellison, Opt. Lett. 12 (10) (1987) 766.
[2] Johannes De Boer, Zhongping Chen, J. Stuart Nelson, et al., Opt. Express 3 (6) (1998) 212.
[3] J. Scott Tyo, Opt. Lett. 25 (16) (2000) 1198.
[4] R. Oldenbourg, G. Mei, J. Microsc. 180 (2) (1995) 140.
[5] K. Oka, T. Kaneko, Opt. Express 11 (13) (2003) 1510.
[6] Y. Ohtsuka, K. Oka, Appl. Opt. 33 (13) (1994) 2633.
[7] E. Cuche, F. Bevilacqua, C. Depeursinge, Opt. Lett. 24 (5) (1999) 291.
[8] T. Colomb, P. Dahlgren, D. Beghuin, et al., Appl. Opt. 41 (1) (2002) 27.
[9] D.S. Kliger, J.W. Lewis, C.E. Randall, Polarized Light in Optics and Spectroscopy, Academic Press, San Diego, 1990 (chapter 5).
[10] Etienne Cuche, Pierre Marquet, Pia Dahlgren, et al., Appl. Opt. 38 (34) (1999) 6994.